# Improved Performance of Dye Sensitized Solar Cells using Ag/Ca doped and co-doped ZnO as Photoanode Materials

KIRTI HOODA[1], ANSHUL SINGH[1,*,iD], VIRENDER SINGH KUNDU[2] and AMAN KUMAR[3]

[1]Department of Chemistry, Baba Mastnath University, Rohtak-124021, India
[2]Department of Electronic Science, Kurukshetra University, Kurukshetra-136119, India
[3]Department of Physics, Maharishi Markandeshwar Deemed to be University, Mullana-133203, India

*Corresponding author: E-mail: anshul9008@gmail.com

An innovative technology for energy harvesting that transforms direct sunlight into electrical energy is dye-sensitized solar cells. Since these cells are flexible, lightweight, inexpensive, environmentally benign and involve a straightforward production method, they have far superior qualities to silicon-based solar cells. Since, a photoanode is the backbone of dye-sensitized solar cell (DSSC), we synthesized ZnO and Ag/Ca doped-codoped ZnO nanoparticles using sol-gel technique. The optical, morphological, and structural characteristics of prepared samples were thoroughly examined. XRD, FESEM-EDX, and UV-Vis were among the methods used to characterize the produced nanoparticles. The X-ray diffraction data showed that the wurtzite structure was single-phase hexagonal and did not contain any impurity phases. The effective integration of Ag/Ca ions into the host ZnO structure is further validated by XRD. Additionally, the XRD investigation demonstrates that the Wurtzite structure of ZnO remains unchanged when Ag/Ca is substituted for ZnO. According to the FESEM morphological images, the produced nanoparticles have a spherical form. The EDAX spectra confirm the presence of Zn, Ca, Ag and O atoms in the samples, while the optical transparency and band gap values were analyzed using UV-Vis spectroscopy. The Co-doping Ca/Ag resulted in a decrease in the energy band gap as determined by Tauc' plot. J-V characterisation was used to assess the electrochemical properties of fill factor, open circuit voltage, and short circuit current density. This signifies a 215.39% enhancement in efficiency compared to the pure ZnO-based photoanode utilized in DSSCs.

**Keywords: Dye sensitized solar cell, Sol-gel, Nanoparticles, Photoanode, J-V characteristics.**

## INTRODUCTION

Solar energy is an abundant, renewable resource that offers a sustainable alternative to conventional fossil fuels. It can be directly converted into electricity without generating carbon emissions, making it an eco-friendly solution to the growing global energy demand. As fossil fuel reserves continue to dwindle, solar energy has garnered significant attention as a viable substitute. Dye-sensitized solar cells (DSSCs) have emerged as a promising technology among various solar energy conversion methods, owing to their cost-effectiveness, ease of fabrication, and scalability for large-scale production. These attributes position DSSCs as a competitive and innovative approach to sustainable energy generation [1-3]. The structure of dye-sensitized solar cells primarily consists of three key components: (i) a dye-sensitized photoanode, which is deposited onto a trans-parent conducting oxide (TCO) substrate such as indium tin oxide (ITO) or fluorine-doped tin oxide (FTO); (ii) an iodide-based electrolyte solution that permeates the photoanode, facilitating charge transport; and (iii) a platinized TCO counter electrode, which serves as the catalytic interface for the redox reaction, ensuring efficient electron transfer within the system.

Incident sunlight is absorbed by the dye molecules, exciting their electrons to a higher energy state. The photo-excited electrons are subsequently transported through an external circuit to the counter electrode (platinized TCO), facilitating the generation of an electric current. Simultaneously, the oxidized dye molecules are restored by the redox electrolyte, which undergoes oxidation at the counter electrode, thereby ensuring the completion of the electrochemical cycle [4]. Titanium dioxide (TiO$_2$) is the most widely utilized photoanode material, esteemed for its extensive availability, high surface area, superior

dye adsorption capacity, exceptional chemical stability and prolonged electron lifetime [5]. It has significant photoelectric characteristics, low manufacturing cost, and adjustable physical properties [6].

Zinc oxide (ZnO) ($E_g$ = 3.37 eV) is readily synthesizable, non-toxic, and exhibits high carrier mobility. Additionally, its nanocrystalline particles demonstrate superior dye adsorption capability [7,8]. Therefore, some reports support that DSSCs with ZnO have better photoelectric efficiency [9]. Nevertheless, ZnO exhibits critical drawbacks such as chemical instability in acidic dye environments, the presence of surface defects, and inefficient electron injection from Ru-based sensitizers [10]; hence, under typical conditions, ZnO-based DSSCs exhibit lower efficiency ($\eta$) compared to TiO$_2$-based DSSCs. To enhance the performance of ZnO-based solar cells, various strategies have been developed [11-14], One approach involves decorating or coating the ZnO nanostructure with other metals or metal oxides, thereby developing nanocomposites with enhanced properties [13,15-21]. The primary constraint of ZnO structures in DSSC applications lies in their restricted absorption within the visible spectrum, predominantly attributed to their intrinsically high absorption in the ultraviolet region and their broad bandgap. To enhance solar energy harvesting efficiency, ZnO structures can be strategically engineered to extend their spectral response, thereby optimizing their photoconversion capabilities and overall device performance. Reducing the bandgap of ZnO structures is a useful approach to improving their absorption in the visible spectrum, which accounts for approximately 43% of solar irradiance. Some of the most effective methods for extending ZnO's optical response into the visible region involves doping its crystal lattice with transition metals, thereby modulating its electronic structure and optimizing its photovoltaic performance [22]. Transition metals are frequently utilized as dopants due to their partially filled *d*- or *f*-orbitals, which facilitate modifications in the electronic and structural properties of ZnO [23]. These dopants play a crucial role in shaping the morphology and particle size of ZnO structures. Specifically, the incorporation of transition metals has been shown to restrict ZnO crystal growth, resulting in smaller nanostructures with an increased surface area, thereby improving their functional properties for optoelectronic applications [24]. Incorporation of transition metals into the ZnO lattice is known to modulate the local Zn environment, thereby altering the electronic band structure and effectively reducing the bandgap. As a result, the optical absorption edge of ZnO moves into the visible light region, enhancing its efficiency in capturing a broader spectrum of solar radiation [25]. Furthermore, metal ion doping enhances the electron transport dynamics within the ZnO framework, facilitating more efficient charge carrier mobility. Moreover, it mitigates the recombination rate between the conduction band of ZnO and the redox electrolyte, thereby improving overall charge separation and photovoltaic performance [26].

Group II elements, such as calcium, magnesium, strontium and barium, are recognized for their high conductivity and their ability to seamlessly integrate into the atomic structure of ZnO. This incorporation induces modifications in both the structural and optical properties of ZnO, including alterations in grain size and bandgap. Doping ZnO nanostructures with these second group elements leads to significant changes in the electronic bandgap as well as the structural morphology of the material, enhancing its functional characteristics.

A variety of advanced techniques are utilized for the synthesis of nanoparticles, including molecular beam epitaxy, metal-organic chemical vapour deposition, plasma-enhanced chemical vapour deposition, sputtering, spray pyrolysis, atomic layer deposition, pulsed laser deposition, electron beam evaporation and the sol-gel process. These methods offers unique advantages for precisely controlling the size, morphology, and composition of nanoparticles in various applications [27]. Compared to the previously described approaches, the sol-gel process offers a number of benefits, including simplicity, affordability, and remarkable efficiency [28]. A sol-gel spin coating approach makes it simple to adjust a number of factors, including the concentration of the precursor solution, the annealing temperature, and the annealing duration in order to obtain the desired results [29].

This study explores the impact of doping or co-doping transition metal elements, specifically silver and an alkali-earth metal, calcium, into a ZnO-based photoanode for dye-sensitized solar cells (DSSCs). The investigation systematically varies the concentrations of Ag and Ca to assess their influence on the material properties. This study represents the first comprehensive investigation into the structural, morphological, optical and photovoltaic properties of Ag- and Ca-doped, as well as co-doped, ZnO, with the objective of optimizing the efficiency of dye-sensitized solar cells (DSSCs). The findings reveal that doping and co-doping with the transition metal Ag significantly enhance charge carrier separation, expedite charge transport, and extend the absorption spectrum into the ultraviolet and near-infrared regions, which were previously unabsorbed. On the other hand doping with alkali earth element improves cell performance by enhancing dye loading on the photoanode. These improvements contribute to an increased efficiency of the investigated dye-sensitized solar cells (DSSCs). The doping and co-doping of Ca or Ag have been found to effectively tackle the challenges associated with ZnO photoanodes in the dye-sensitized solar cells (DSSCs), resulting in a substantial enhancement of the device's performance. By adjusting the dopant concentration, sol-gel nanoparticles were created and successfully used as a photoanode. Ruthenium N719 dye was chosen since it is one of the most effective dyes for DSSC because of its capacity to absorb visible light and its special qualities, which include stable anchoring to the ZnO surface and rapid electron injection.

## EXPERIMENTAL

Zinc nitrate dihydrate [Zn(NO$_3$)$_2$·2H$_2$O], silver nitrate [Ag(NO$_3$)], calcium chloride dihydrate [CaCl$_2$·2H$_2$O], sodium hydroxide, ammonium hydroxide, ethanol, acetone, isopropyl alcohol, Triton X-100, fluorine doped tin oxide (FTO), iodine, potassium iodide and ethylene glycol. All used chemicals were procured from Sigma-Aldrich and were of AR Grade.

**Synthesis of nanoparticles:** All the reagents, zinc nitrate dehydrate [$Zn(NO_3)_2 \cdot 2H_2O$], silver nitrate [$Ag(NO_3)$], calcium chloride dihydrate [$CaCl_2 \cdot 2H_2O$] were taken as starting material. Sol-gel technique was used to prepare (i) bare ZnO *i.e.* $Zn_{1.0}O$ Zn-29.74 g (wt.%), (ii) Ca-doped ZnO ($Zn_{0.85}Ca_{0.15}O$) Zn-25.2 g, Ca-2.20 g (wt.%), (iii) Ag doped ZnO ($Zn_{0.85}Ag_{0.15}O$) Zn-25.2 g, Cu-2.54 g and (iv) Ca/Ag co-doped ZnO ($Zn_{0.85}Ca_{0.075}Ag_{0.075}O$) Zn-25.2 g, Ca-1.10 g, Ag-2.54 g (wt.%) nanoparticles. These compounds were dissolved in 100 mL of deionized water while being vigorously stirred for around 4 h. Ammonia solution was added dropwise while being continuously stirred at 60 °C for 1 h or until the pH of the reaction mixture reached 8. The well blended solution turned thicker attaining the consistency of a thick gel after being agitated for an entire hour. The resulting gel was washed with de-ionized water. Then, the gel was allowed to calcine for about 3 h at 350 °C. The designation and compositional details of the synthesized samples are presented in Table-1. Initially, pristine ZnO nanoparticles were synthesized, followed by doping with Ag and Ca at varying concentrations to enhance their properties. The simple and efficient synthesis of ZnO nanoparticles using the sol-gel method is attributed due to the underlying chemical reaction, which facilitates the formation of ZnO from precursor materials under controlled conditions [30].
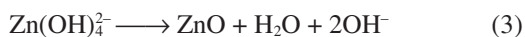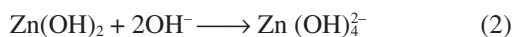
$$Zn^{2+} + 2OH^- \longrightarrow Zn(OH)_2 \qquad (1)$$

$$Zn(OH)_2 + 2OH^- \longrightarrow Zn(OH)_4^{2-} \qquad (2)$$

$$Zn(OH)_4^{2-} \longrightarrow ZnO + H_2O + 2OH^- \qquad (3)$$

**TABLE-1**
**SAMPLE CODE AND COMPOSITION OF AS SYNTHESIZED Ag/Ca-ZnO NANOPARTICLES**

| Sample No. | Sample code | Sample composition |
|---|---|---|
| 1 | ZO | $Zn_{1.0}O$ |
| 2 | CZO | $Zn_{0.85}Ca_{0.15}O$ |
| 3 | AZO | $Zn_{0.85}Ag_{0.85}O$ |
| 4 | CAZO | $Zn_{0.85}Ca_{0.075}Ag_{0.075}O$ |

**Fabrication of dye sensitized solar cell**

**Dye:** N719 *i.e.* di-tetrabutylammoniumcis-*bis*(isothiocyanato)*bis*(2,2′-bipyridyl-4,4′-dicarboxylato) ruthenium(II) a high performance dye is the ammonium salt of N3 dye. It is a modified dye that increases the device voltage and was used here to fabricate photoanode for DSSS's.

**Preparation of photoanode utilizing fluorine doped tin oxide glass sheets:** The photoanodes were fabricated using FTO-coated conducting glass substrates, which were initially undergone a thorough cleaning process by immersing them in an ultrasonic bath containing soapy water, followed by thorough rinsing with distilled water and ethanol. After the cleaning, the FTO coated conducting glass sheets were dried and further used for the preparation of photoanodes. During this procedure, the FTO glass was cross-sectioned into 3 cm × 3 cm pieces and subsequently cleaned using a combination of detergent, acetone and deionized water. These pieces were then placed in a sonicator for about 10 min and dried with a hair dryer.

The process of testing the conducting side of FTO involved using a multimeter to measure its electrical conductivity and then marking an appropriate (1cm × 1cm) dimension on it. To ensure perfection, a tape was used to mask the substrate, adhering to the measured dimensions of the photoanode. A homogenous paste was than prepared by adding an appropriate quantity of powdered sample to ethanol, which was mixed until a uniform consistency was achieved. To ensure even coverage on the FTO substrate, Triton X-100 was used as a surfactant. The paste was subsequently spread uniformly onto the FTO substrate using the doctor-blade method. Four working electrodes were simultaneously prepared using this method. The prepared photoanodes were subsequently placed in a muffle furnace and heated at 400 °C for 35 min. After the heating process, the photoanodes were immersed in a Ruthenium N719 dye solution for sensitization.

**Preparation of electrolyte:** Iodide tri-iodide ($I^-/I_3^-$) was employed as an electrolyte to facilitate conduction between the counter electrode and the photoanode. Begin by measuring 10 mL of ethylene glycol. Next, added 0.83 g of KI and 0.127 g of iodine ($I_2$) to the solution. All the reagents should be thoroughly mixed in a beaker to ensure homogeneity. The resulting solution should then be stored in an opaque container to protect it from direct exposure to solar radiation.

**Counter electrode preparation:** The conductive surface of the FTO was determined with a voltmeter, followed by the application of a carbon coating using a graphite pencil. The lead pencil was evenly distributed throughout the whole FTO surface in order to prepare a steady and continuous carbon coating.

**Assembly of DSSC:** Upon completion of the preparation of all components of the DSSC, the photoanode was submerged in a dye solution for 24 h. Following this, the photoanode was carefully rinsed with deionized water and permitted to dry. The DSSC was constructed by applying multiple drops of electrolyte to the photoanode, after which the photoanode FTO was secured to the counter electrode FTO using a binding clip. A solar simulator was employed to assess the I-V characteristics of the assembled DSSCs.

**Characterization:** The crystalline structure, grain size and composition of ZnO doped and co-doped Ca/Ag nanoparticles were analyzed using a PANalytical X'Pert Pro diffractometer. The measurements were conducted with Cu-$K\alpha$ radiation at a wavelength of $\lambda = 1.54056$ Å, under conditions of 45 kV and 40 mA, to assess the crystalline characteristics of the samples. A Perkin-Elmer Lambda 650 was used for UV-visible spectroscopy in order to determine the bandgap energies and examine the absorption characteristics of various photoanodes. Tauc plot analysis was used to establish the bandgap values for both doped and undoped materials. The wavelength range in which the UV absorption spectrophotometer operated was 190 nm to 900 nm. The surface morphologies were analyzed by using JEOL JSM-7610FPlus Field Emission Scanning Electron Microscope. Furthermore, elemental composition analysis of the sample surfaces was undertaken using the integrated Energy Dispersive X-ray Spectroscopy (EDX) system within the FESEM setup.

**Photovoltaic characterization:** The assembled solar cell was evaluated for its current-voltage performance under dark conditions using an Oriel Solar Simulator (AM 1.5, 100 mW/cm$^2$), Oriel Sol3A Newport, and a Keithley 2400 source measure unit. The photovoltaic current density-voltage characterization was subsequently performed to assess the cell's electrical behaviour.

## RESULTS AND DISCUSSION

**XRD analysis:** The crystallinity and the particle sizes of ZnO, ZnCaO, ZnAgO and ZnCaAgO nanoparticles were analyzed using the XRD. The X-ray diffraction patterns of bare, Ca/Ag-doped and co-doped ZnO nanoparticles on an FTO substrate are displayed in Fig. 1. According to the figure, the addition of Ca/Ag using the JCPDS database of card 36-1451 [31] results in polycrystalline films with a hexagonal wurtzite structure with no additional phases. A high level of crystallinity is indicated by the nine sharp and intense ZnO peaks found in all samples ((100), (002), (101), (102), (110), (103), (200), (112) and (201). The XRD spectrum reveals the absence of peaks corresponding to Ca or Ag ions, suggesting that the incorporation of Cu or these ions does not alter the hexagonal wurtzite structure [32]. The crystallite size of the synthesized particles was determined using the Debye-Scherrer equation (4), which relies on the line broadening (full-width at half-maximum, FWHM) of the (101) diffraction peak [33].

$$D = \frac{0.94\lambda}{\beta\cos\theta} \tag{4}$$

where θ is the Bragg angle (°), β is the full half maximum, FWHM (radian), λ is the wavelength and D is the crystallite size (nm).
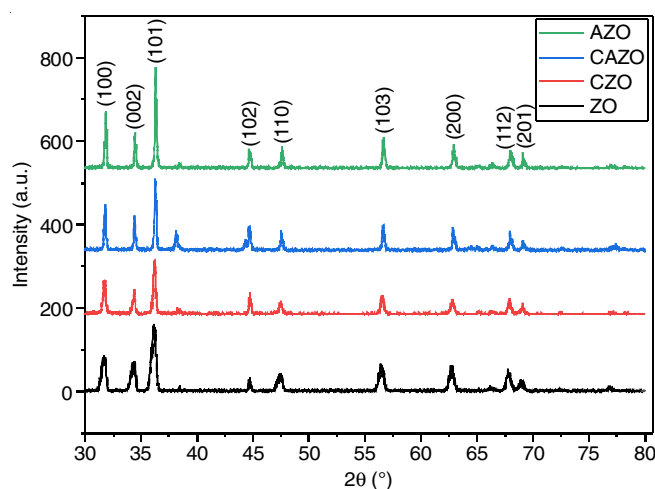


Fig. 1. X-ray diffraction pattern for synthesized nanoparticles

Moreover, using Bragg's rule, a number of other parameters, such as d-spacing and lattice strain, were determined [34,35] using the obtained XRD data and are reported in Table-2.

$$\text{Lattice strain } (\varepsilon) = \frac{\beta}{4\tan\theta} \tag{5}$$

$$\text{d-spacing } (d) = \frac{n\lambda}{2\sin\theta} \tag{6}$$

where FWHM and θ have same value mentioned above. The computed values are presented in Table-2.

The crystallite sizes of the synthesized samples-ZO, CZO, AZO, and CAZO were determined to be 12.985 nm, 22.900 nm, 22.726 nm and 15.152 nm, respectively, reflecting the variations in their crystalline structure, indicating distinct variations in their crystalline structure. When compared to the bare sample, the increased crystallite size indicates that the atoms are more organized in their orientation.

**UV-visible spectra analysis:** In this study, pristine ZnO and Ca/Ag-doped ZnO nanoparticles were synthesized. UV-visible spectroscopy was utilized to investigate the absorbance characteristics and bandgap energies of bare ZnO, ZnO nanoparticles doped with Ca or Ag, and co-doped ZnO (Ca/Ag) within the wavelength range of 300-800 nm [36]. Fig. 2 shows the UV-Vis spectra of ZnO and Ca/Ag-doped ZnO nanoparticles. The synthesized ZnO nanoparticles exhibit a wurtzite crystal structure, as evidenced by the UV absorption edge observed at 364 nm. The incorporation of Ca and Ag into the ZnO lattice induces a red shift in the absorption edge, indicating structural modifications in the pristine ZnO framework. The incorporation of Ca into ZnO has the potential to shift its photon absorption capability from the ultraviolet (UV) to the visible region, thereby expanding its absorption spectrum. The UV spectroscopy data further reveal the absence of distinct peaks corresponding to AgNO?. This is attributed to the fact that AgNO$_3$, being an ionic compound rather than an intrinsically coloured material, exhibits a pale-yellow colour in solution rather than distinct absorption features. The absorption of ultraviolet and visible light by molecules, inducing the excitation of electrons from lower to higher energy states. As silver nitrate is an ionic compound lacking conjugated π-bonds, it is incapable of absorbing UV or visible light, as its electronic structure does not support such transitions [37].

The band gap energy for all samples was determined utilizing the Tauc plot based on Tauc's relation [38].

$$(\alpha h\nu) = C(h\nu - E_g)^n \tag{7}$$

where n takes the values of 1/2, 3/2, 2 and 3 for direct allowed transitions, direct forbidden transitions and indirect allowed transitions, respectively; h represents Planck's constant; C

| | | TABLE-2 | | | |
|---|---|---|---|---|---|
| | | VARIOUS CALCULATED/OBSERVED STRUCTURAL PARAMETERS FROM XRD | | | |
| Sample composition | Diffraction angle* (2θ) | FWHM* | Crystallite size* (nm) | Lattice strain* (Є) | d-spacing* |
| $Zn_{1.0}O$ | 36.211 | 0.672 | 12.985 | 0.00897 | 1.3000 |
| $Zn_{0.85}Ca_{0.15}O$ | 36.172 | 0.381 | 22.900 | 0.00500 | 1.3046 |
| $Zn_{0.85}Ag_{0.15}O$ | 36.244 | 0.384 | 22.726 | 0.00510 | 1.3024 |
| $Zn_{0.85}Ca_{0.075}Ag_{0.075}O$ | 36.280 | 0.576 | 15.152 | 0.00760 | 1.3013 |

*Parameters corresponding peaks of 100% relative intensities, cooperating well with Fig. 1.
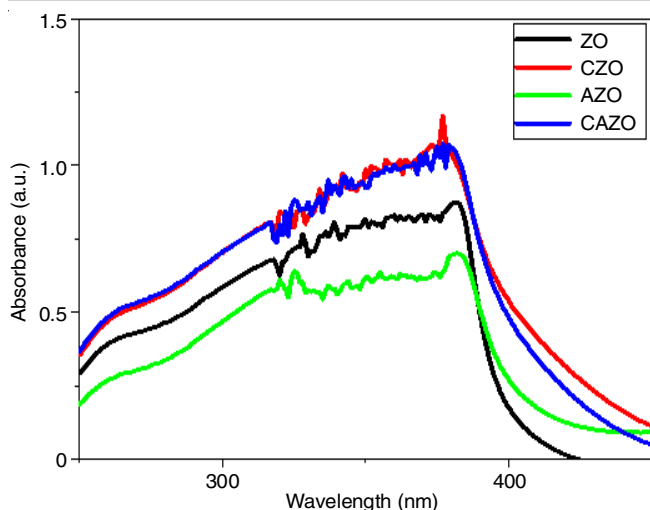
Fig. 2. Optical absorbance spectra of as studied samples

denotes the proportionality constant; $\nu$ is the frequency of incident light; $\alpha$ signifies the absorption coefficient; and $E_g$ refers to the optical bandgap energy. The observed optical band gap ($E_g$) values are 2.94eV, 2.90eV, 2.86eV and 2.92eV, as shown in Fig. 3. Doping ZnO with Ca/Ag results in the reduction of bandgap, which is possibly due to the introduction of defect states as Ag doping creates localized states near the conduction band or valence band. These states facilitate electronic transitions at lower energies, effectively curtailing the bandgap whereas Ca doping introduces oxygen vacancies or other defects that contribute mid-gap states, helping in bandgap reduction. Co-

doping results in a noticeable redshift in the absorption edge, indicating reduced bandgap energy [39]. The combined doping of Ag and Ca modifies the ZnO lattice, developing a more substantial shift in the electronic band structure than individual doping. The defects and states introduced by Ag and Ca overlap, enhancing their impact on bandgap narrowing [40].
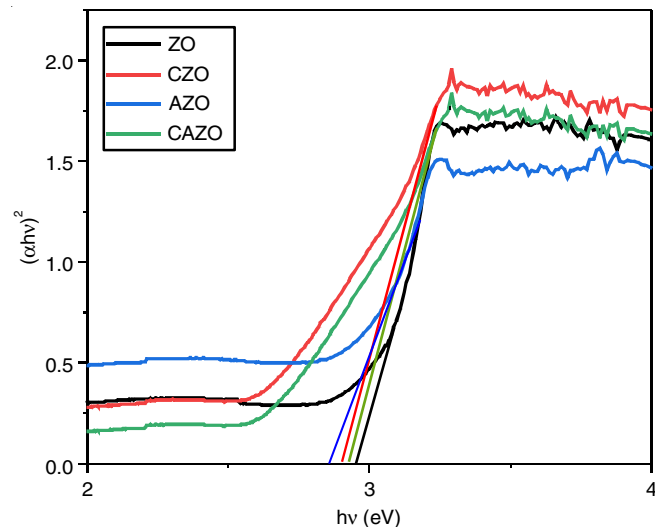


Fig. 3. Tauc plot of various prepared samples

**FESEM:** Fig. 4 presents the FESEM images and surface morphology of bare, doped and co-doped Ag/Ca ZnO nanoparticles in panels (a-d). Undoped ZnO nanoparticles typically
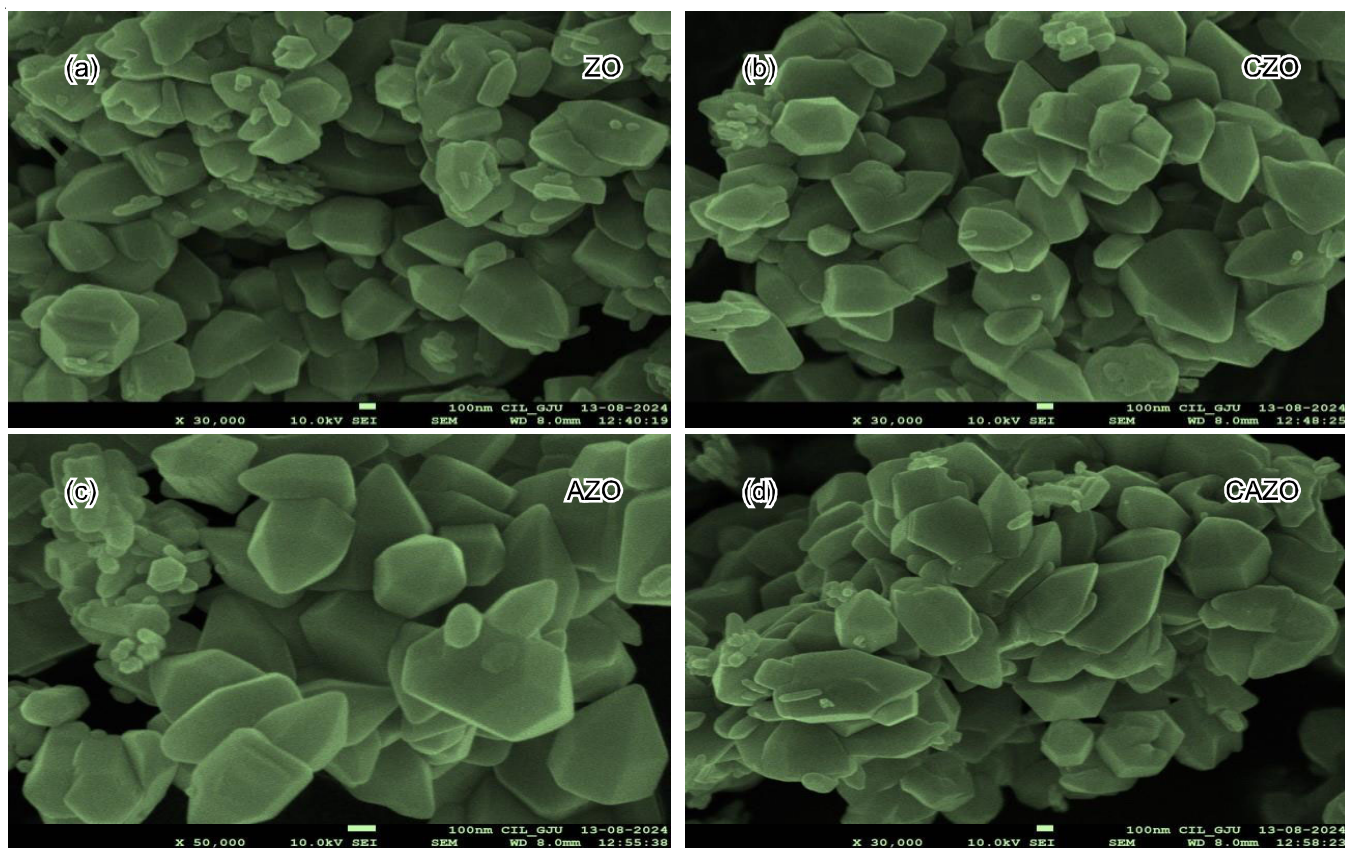


Fig. 4. FESEM micrographs of the samples (a) ZO (b) CZO (c) AZO and (d) CAZO

exhibit a hexagonal Wurtzite structure, with morphologies such as rods, spheres or flakes. The addition of Ag and Ca as dopants often alters the morphology due to change in the growth kinetics and lattice structure during synthesis. Ag/Ca doping reduced particle agglomeration and enhanced surface uniformity in ZnO nanoparticles, with improved spherical shapes compared to undoped ZnO. This was attributed to the influence of dopants on nucleation and growth mechanisms during synthesis [41]. FESEM images typically show that doping with Ca and Ag reduces the particle size due to the inhibition of grain growth. The Ca/Ag co-doping promote better surface uniformity, which is desirable for optical and electronic applications [42].

**Energy dispersive spectroscopy (EDS):** The composition of the dopants within the host ZnO was revealed by Fig. 5 while Table-3 presents the EDS spectra of Ag/Ca doped and co-doped ZnO, along with their respective concentrations expressed in atomic percent. EDS also detect unintended elements or impurities that might have been introduced during synthesis. No unexpected peaks observed resulting in a high-purity sample. Additional peaks for Ag and Ca validate successful doping. Peak of Ag (L$\alpha$) around 2.98 KeV and peak of Ca around 3.69 KeV confirms their further incorporation into ZnO matrix, which was found to be aligned with the literature [43]. Doping was also confirmed by the atomic percentage of each dopant present in the host matrix, relative doping percentage fairly line up with the intented doping concentration.

### TABLE-3
### CHEMICAL COMPOSITION OF SAMPLES ZO, CZO, AZO, AND CAZO OBSERVED FROM EDS ANALYSIS

| Sample | Zinc (at.%) | Calcium (at.%) | Silver (at.%) | Oxygen (at.%) |
|--------|-------------|----------------|---------------|---------------|
| ZO | 41.07 | – | – | 58.93 |
| CZO | 32.56 | 7.23 | – | 60.21 |
| AZO | 37.94 | – | 8.47 | 53.58 |
| CAZO | 36.60 | 3.27 | 0.03 | 60.17 |

**J-V measurement:** Co-doping ZnO with silver and calcium enhances the efficiency of dye-sensitized solar cells due to the improvements in optical, electronic and structural properties. The synergy between silver and calcium significantly impacts the power conversion efficiency (PCE) by influencing factors like light absorption, electron transport and charge recombination. In order to investigate the performance variations caused by Mg/Cu doping and co-doping, ZnO and doped photoanodes (ZO, CZO, AZO and CAZO) were assembled into DSSCs. Under AM 1.5, 100 mW cm$^{-2}$ light irradiation, the performance of these four photoanode series was tested and presented in Fig. 6, with comprehensive characteristics listed in Table-4. The fill factor (FF) and efficiency ($\eta$) of dye-sensitized solar cells (DSSCs) are ascertained through the application of the following formulae:

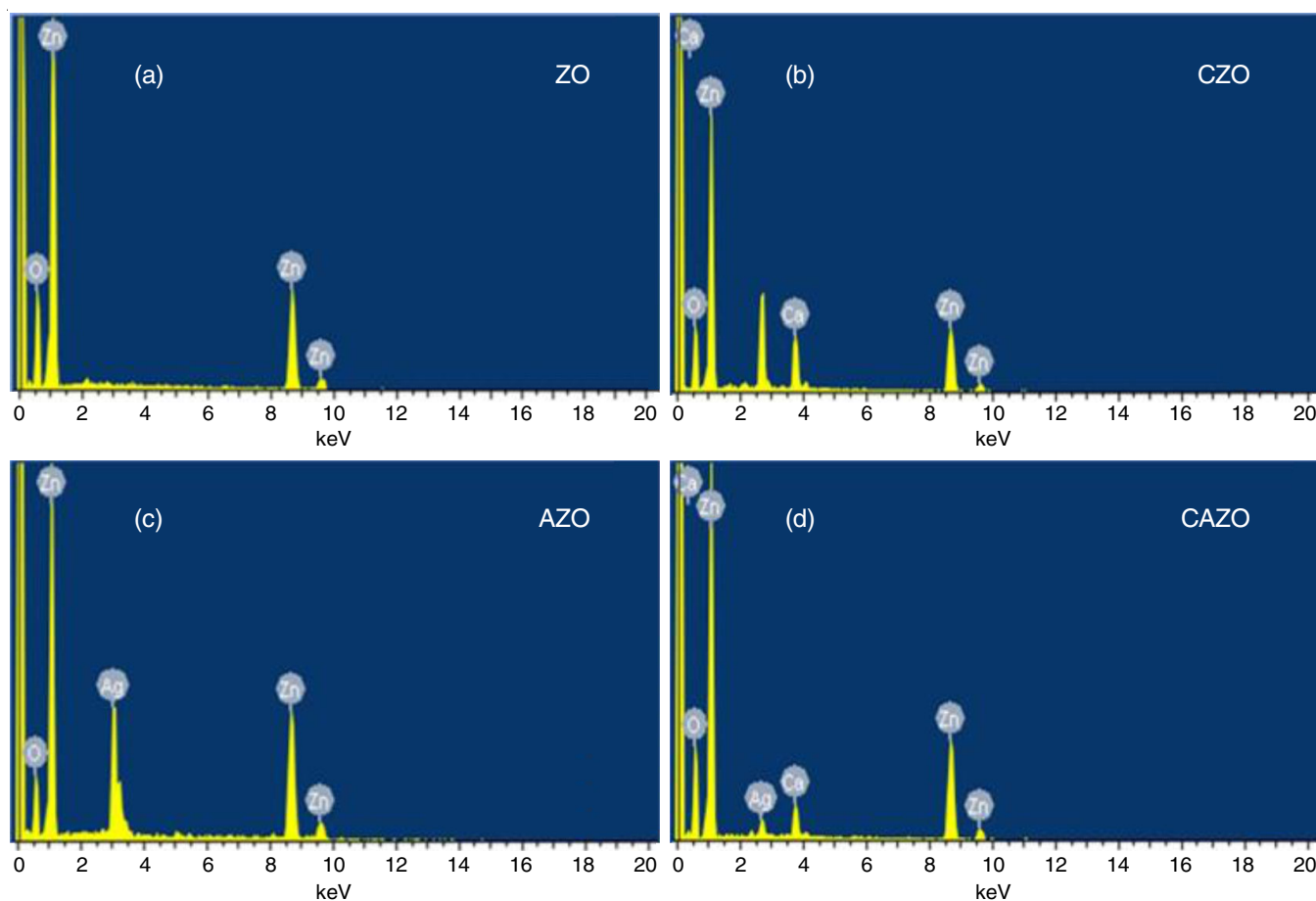$$FF = \frac{J_{max} \times V_{max}}{J_{sc} \times V_{oc}} \qquad (8)$$



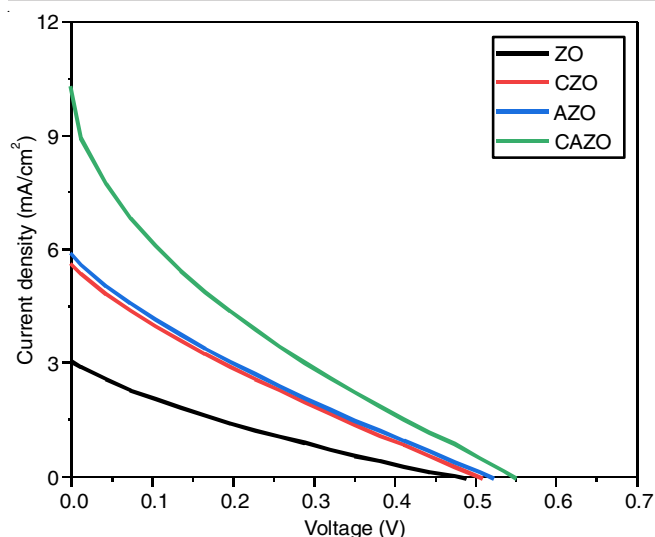Fig. 5. EDX images of samples (a) ZO, (b) CZO, (c) AZO and (d) CAZO

Fig. 6. J-V curve of ZO, CZO, AZO and CAZO photoanode based DSSC

TABLE-4
DIFFERENT PHOTOVOLTAIC PARAMETERS
FOR ALL THE FABRICATED DSSCs

| Sample | $J_{sc}$ (mA/cm$^2$) | $V_{oc}$ (V) | FF | Efficiency |
|---|---|---|---|---|
| ZO | 3.087 | 0.473 | 19.32 | 0.2826 |
| CZO | 5.662 | 0.500 | 20.83 | 0.5908 |
| AZO | 5.963 | 0.515 | 20.13 | 0.6192 |
| CAZO | 10.801 | 0.544 | 15.16 | 0.8913 |

$$\eta = \frac{(J_{sc} \times V_{oc} \times FF)}{P_{in}} \qquad (9)$$

Based on the recorded of J-V curve, the open-circuit voltage ($V_{oc}$) and short-circuit current density ($J_{sc}$) were determined. The bare ZnO photoanode based DSSC exhibits $V_{oc}$, $J_{sc}$, FF and $\eta$ values of 0.473V, 3.087 mA/cm$^2$, 19.32 and 0.2826%, respectively. In case of Ca doped ZnO based DSSC, the photovoltaic parameters of $V_{oc}$ and $J_{sc}$ increases to 0.500 V and 5.662 mA/cm$^2$, respectively, resulting in an increased $\eta$ value of 0.5908%. Similarly, Ag doped ZnO based DSSC leads to an escalation in the values of $V_{oc}$ and $J_{sc}$ to 0.515V and 5.963 mA/cm$^2$, respectively, resulting in an increased $\eta$ value of 0.6192%. Furthermore, calcium and silver co-doped ZnO photoanode based DSSC shows enhancement of the photovoltaic parameters, with the values of $V_{oc}$ and $J_{sc}$ upsurging to 0.544 V and 10.801 mA/cm$^2$, respectively. This results in an increased $\eta$ value of 0.8913% as listed in Table-4.

This improvement in efficiency of co-doped nanoparticles used as photoanode may be due to the co-doping of ZnO with silver and calcium, which introduces significant improvements in optical, electronic and structural properties, directly enhancing the power conversion efficiency (PCE). Silver and calcium co-doping reduces the bandgap of ZnO, enabling the material to absorb more light in the visible region. Silver introduces localized surface plasmon resonance (LSPR), while calcium induces structural and electronic changes, extending light absorption to lower energy region. Broader light absorption results in higher photocurrent generation and improved short-circuit current density ($J_{sc}$) [44]. Silver introduces trap states in ZnO that facilitate electron transport within the conduction band.

The plasmonic effects from silver enhance hot electron generation and injection into ZnO. Ca reduces grain boundary resistance and improves the ZnO crystallinity, allowing for faster electron movement; reduces oxygen vacancies, minimizing charge recombination. Better electron mobility and reduced recombination lead to higher open-circuit voltage ($V_{oc}$) and fill factor (FF) [45]. Co-doping ZnO with silver and calcium leads to the synergistic effects that significantly enhance the performance of dye-sensitized solar cells (DSSCs). Consequently, the co-doped sample surpasses the limitations associated with bare ZnO, demonstrating a maximum efficiency increase of 215.39% compared to bare ZnO.

**Conclusion**

Ca-Ag co-doped nanoparticles were synthesized through the sol-gel method and subsequently integrated into a photoanode *via* the doctor-blade technique. Ruthenium N719 dye was utilized as sensitizer, the synthesized nanoparticles were then characterized using X-ray diffraction (XRD), UV-Visible (UV-Vis) spectroscopy, field emission scanning electron microscopy (FESEM) and energy dispersive X-ray (EDX) analysis to investigate their crystalline structure, optical properties, band gap, and morphology. Current-voltage (I-V) measurements were conducted to assess the overall efficiency of the fabricated DSSC. XRD analysis revealed that Ca-Ag co-doping in ZnO preserves the hexagonal wurtzite structure of the material. Enhanced crystallinity improves charge carrier mobility and over all photovoltaic performance. Silver-calcium co-doping reduces the bandgap of ZnO extending the light absorption into the visible region, which intern improved short circuit current density. Surface morphology of synthesized material found with reduced size and higher surface area, beneficial for the dye absorption. The plasmonic effect of silver improved light absorption and electron injection, whereas calcium enhances electron mobility and reduces recombination. Combined effect results in the enhancement of power conversion efficiency (PCE) upto 215.39%, making them promising material for high performance DSSC.

### CONFLICT OF INTEREST

The authors declare that there is no conflict of interests regarding the publication of this article.

### REFERENCES

1.  A. Hagfeldt, G. Boschloo, L. Sun, L. Kloo and H. Pettersson, *Chem. Rev.*, **110**, 6595 (2010);
    https://doi.org/10.1021/cr900356p

2.  J. Gong, K. Sumathy, Q. Qiao and Z. Zhou, *Renew. Sustain. Energy Rev.*, **68**, 234 (2017);
    https://doi.org/10.1016/j.rser.2016.09.097

3.  A.B. Muñoz-García, I. Benesperi, G. Boschloo, J.J. Concepcion, J.H. Delcamp, E.A. Gibson, G.J. Meyer, M. Pavone, H. Pettersson, A. Hagfeldt and M. Freitag, *Chem. Soc. Rev.*, **50**, 12450 (2021);
    https://doi.org/10.1039/D0CS01336F

4. J.H. Yum, E. Baranoff, S. Wenger, M.K. Nazeeruddin and M. Grätzel, *Energy Environ. Sci.*, **4**, 842 (2011); https://doi.org/10.1039/C0EE00536C

5. S. Suhaimi, M.M. Shahimin, Z.A. Alahmed, J. Chysky and A.H. Reshak, *Int. J. Electrochem. Sci.*, **10**, 2859 (2015); https://doi.org/10.1016/S1452-3981(23)06503-3

6. N.G. Park, M.G. Kang, K.M. Kim, K.S. Ryu, S.H. Chang, D.-K. Kim, J. van de Lagemaat, K.D. Benkstein and A.J. Frank, *Langmuir*, **20**, 4246 (2004); https://doi.org/10.1021/la036122x

7. S. Raha and M. Ahmaruzzaman, *Nanoscale Adv.*, **4**, 1868 (2022); https://doi.org/10.1039/D1NA00880C

8. S.S. Kanmani and K. Ramachandran, *Renew. Energy*, **43**, 149 (2012); https://doi.org/10.1016/j.renene.2011.12.014

9. N. Sakai, T. Miyasaka and T.N. Murakami, *J. Phys. Chem. C*, **117**, 10949 (2013); https://doi.org/10.1021/jp401106u

10. J. Jung, J. Myoung and S. Lim, *Thin Solid Films*, **520**, 5779 (2012); https://doi.org/10.1016/j.tsf.2012.04.052

11. M.B. Tahir, H. Javad, K. Nadeem and A. Majid, *Surf. Rev. Lett.*, **25**, 1930001 (2018); https://doi.org/10.1142/S0218625X19300016

12. R. Kumar, A. Umar, G. Kumar, H.S. Nalwa, A. Kumar and M.S. Akhtar, *J. Mater. Sci.*, **52**, 4743 (2017); https://doi.org/10.1007/s10853-016-0668-z

13. B. Boro, B. Gogoi, B.M. Rajbongshi and A. Ramchiary, *Renew. Sustain. Energy Rev.*, **81**, 2264 (2018); https://doi.org/10.1016/j.rser.2017.06.035

14. R. Vittal and K.C. Ho, *Renew. Sustain. Energy Rev.*, **70**, 920 (2017); https://doi.org/10.1016/j.rser.2016.11.273

15. M. Law, L.E. Greene, A. Radenovic, T. Kuykendall, J. Liphardt and P. Yang, *J. Phys. Chem. B*, **110**, 22652 (2006); https://doi.org/10.1021/jp0648644

16. A.S. Mokrushin, I.A. Nagornov, Y.M. Gorban, S.A. Dmitrieva, T.L. Simonenko, N.P. Simonenko, M.S. Doronina, I.R. Vakhitov, M.S. Nikitenko, D.Y. Khudonogov, O.V. Vershinina and E.P. Simonenko, J. Alloys Comp., 1009, 176856 (2024); https://doi.org/10.1016/j.jallcom.2024.176856

17. M. Kaur and N.K. Verma, *J. Mater. Sci. Mater. Electron.*, **24**, 3617 (2013); https://doi.org/10.1007/s10854-013-1293-0

18. G. Divitini, N.O.V. Plank, H.J. Snaith, M.E. Welland and C. Ducati, *J. Phys. Conf. Ser.*, **241**, 012031 (2010); https://doi.org/10.1088/1742-6596/241/1/012031

19. N.O.V. Plank, H.J. Snaith, C. Ducati, J.S. Bendall, L. Schmidt-Mende and M.E. Welland, *Nanotechnology*, **19**, 465603 (2008); https://doi.org/10.1088/0957-4484/19/46/465603

20. S. Nilphai, M. Thepnurat, N. Hongsith, S. Phadungdhitidhada, P. Ruankham, A. Gardchareon, D. Wongratanaphisan and S. Choopun, *Key Eng. Mater.*, **675-676**, 158 (2016); https://doi.org/10.4028/www.scientific.net/KEM.675-676.158

21. M. Kaur and N.K. Verma, *J. Mater. Sci. Mater. Electron.*, **24**, 4980 (2013); https://doi.org/10.1007/s10854-013-1512-8

22. S. Rehman, R. Ullah, A.M. Butt and N.D. Gohar, *J. Hazard. Mater.*, **170**, 560 (2009); https://doi.org/10.1016/j.jhazmat.2009.05.064

23. Y. Peng, S. Qin, W.-S. Wang and A.-W. Xu, *CrystEngComm*, **15**, 6518 (2013); https://doi.org/10.1039/c3ce40798e

24. K.C. Barick, S. Singh, M. Aslam and D. Bahadur, *Micropor. Mesopor. Mater.*, **134**, 195 (2010); https://doi.org/10.1016/j.micromeso.2010.05.026

25. A.M. Toufiq, R. Hussain, A. Shah, A. Mahmood, A. Rehman, A. Khan and S. Rahman, *Physica B*, **604**, 412731 (2021); https://doi.org/10.1016/j.physb.2020.412731

26. E. Akman, *J. Mol. Liq.*, **317**, 114223 (2020); https://doi.org/10.1016/j.molliq.2020.114223

27. D. Escorcia-Díaz, S. García-Mora, L. Rendón-Castrillón, M. Ramírez-Carmona and C. Ocampo-López, *Nanomaterials*, **13**, 2586 (2023); https://doi.org/10.3390/nano13182586

28. F. Aslan, A. Tumbul, A. Göktas, R. Budakoglu and I.H. Mutlu, *J. Sol-Gel Sci. Technol.*, **80**, 389 (2016); https://doi.org/10.1007/s10971-016-4131-z

29. M.N.H. Mia, M.F. Pervez, M.K. Hossain, M. Reefaz Rahman, M. Uddin, M. Jalal and M.A. Al Mashud, *Results Phys.*, **7**, 2683 (2017); https://doi.org/10.1016/j.rinp.2017.07.047

30. V. Cauda, D. Pugliese, N. Garino, A. Sacco, S. Bianco, F. Bella, A. Lamberti and C. Gerbaldi, *Energy*, **65**, 639 (2014); https://doi.org/10.1016/j.energy.2013.12.025

31. N.S. Gultom, H. Abdullah and D.-H. Kuo, *Appl. Catal. B*, **272**, 118985 (2020); https://doi.org/10.1016/j.apcatb.2020.118985

32. H.A.H. Alshamsi and B.S. Hussein, *Orient. J. Chem.*, **34**, 1898 (2018); https://doi.org/10.13005/ojc/3404025

33. M. Mujahid and O.A. Al-Hartomy, *Mater. Res. Innov.*, **27**, 194 (2023); https://doi.org/10.1080/14328917.2022.2113270

34. M. Amjad, M.I. Khan, N. Alwadai, M. Irfan, Ikram-ul-Haq, H. Albalawi, A.H. Almuqrin, M.M. Almoneef and M. Iqbal, *Nanomaterials*, **12**, 1057 (2022); https://doi.org/10.3390/nano12071057

35. J. Chauhan, N. Srivastav, A. Dugaya and D. Pandey, *MOJ Polym. Sci.*, **1**, 26 (2017); https://doi.org/10.15406/mojps.2017.01.00005

36. T. Munir, M. Kashif, K. Mahmood, M. Imran, A. Ali, N. Sabir, N. Amin, A. Mahmood, H. Ali and N. Ahmed, *J. Ovonic Res.*, **15**, 173 (2019).

37. A. Hussain, S. Fiaz, A. Almohammedi and A. Waqar, *Heliyon*, **10**, e35725 (2024); https://doi.org/10.1016/j.heliyon.2024.e35725

38. B.D. Viezbicke, S. Patel, B.E. Davis and D.P. Birnie III, *Phys. Status Solidii, B Basic Res.*, **252**, 1700 (2015); https://doi.org/10.1002/pssb.201552007

39. Q. Deng, X. Han, Y. Gao and G. Shao, *J. Appl. Phys.*, **112**, 013523 (2012); https://doi.org/10.1063/1.4733971

40. S. Al-Ariki, N.A.A. Yahya, S.A. Al-A'nsi, M.H.H. Jumali, A.N. Jannah and R. Abd-Shukor, *Sci. Rep.*, **11**, 11948 (2021); https://doi.org/10.1038/s41598-021-91439-1

41. S. Baruah and J. Dutta, *Sci. Technol. Adv. Mater.*, **10**, 013001 (2009); https://doi.org/10.1088/1468-6996/10/1/013001

42. H..A.O. Alkhayatt, *J. Kufa – Phys.* **9(2)**, 41-55 (2017); https://doi.org/10.31257/2018/JKP/2017/v9.i2.9419

43. S.M. Hosseini, I.A. Sarsari, P. Kameli and H. Salamati, *J. Alloys Compd.*, **640**, 408 (2015); https://doi.org/10.1016/j.jallcom.2015.03.136

44. N.L. Tarwal, V.L. Patil, J.R. Rani, K.V. Gurav, M.S. Khandekar, N.S. Harale, J.S. Shaikh, P.S. Patil and J.H. Jang, *Chinese J. Phys.*, **73**, 581 (2021); https://doi.org/10.1016/j.cjph.2021.03.031

45. K.N. Ganesha, H. Chandrappa, S.R. Kumarswamy, V. Annadurai, H. Somashekarappa and R Somashekar, *Non-Metallic Mater. Sci.*, **5**, 49 (2023); https://doi.org/10.30564/nmms.v5i1.5677